The Astrophysical Journal, 732:98 (8pp), 2011 May 10 doi:10.1088/0004-637X/732/2/98

DUST EMISSION FROM EVOLVED AND UNEVOLVED H II REGIONS IN THE LARGE MAGELLANIC CLOUD

C. T. Slater[1], M. S. Oey[1], A. Li[2], J.-Ph. Bernard[3,4], E. Churchwell[5], K. D. Gordon[6], R. Indebetouw[7,8], B. Lawton[6], M. Meixner[6], D. Paradis[3,4], and W.T. Reach[9]

[1] Astronomy Department, University of Michigan, Ann Arbor, MI 48109, USA
[2] Department of Physics and Astronomy, University of Missouri, Columbia, MO 65211, USA
[3] Universit de Toulouse, UPS-OMP, IRAP, Toulouse, France
[4] CNRS, IRAP, 9 Av. colonel Roche, BP 44346, F-31028 Toulouse Cedex 4, France
[5] Department of Astronomy, University of Wisconsin-Madison, 475 North Charter Street, Madison, WI 53706, USA
[6] Space Telescope Science Institute, 3700 San Martin Drive, Baltimore, MD 21218, USA
[7] Department of Astronomy, University of Virginia, P.O. Box 3818, Charlottesville, VA 22903, USA
[8] National Radio Astronomy Observatory, 520 Edgemont Road, Charlottesville, VA 22903, USA
[9] Universities Space Research Association, Stratospheric Observatory for Infrared Astronomy, NASA Ames Research Center, MS 211-3, Moffett Field, CA 94035, USA

Received 2011 January 10; accepted 2011 March 7; published 2011 April 21

ABSTRACT

We present a study of the dust properties of 12 classical and superbubble H II regions in the Large Magellanic Cloud. We use infrared photometry from *Spitzer* (8, 24, 70, and 160 μm bands), obtained as part of the Surveying the Agents of a Galaxy's Evolution (SAGE) program, along with archival spectroscopic classifications of the ionizing stars to examine the role of stellar sources on dust heating and processing. Our infrared observations show surprisingly little correlation between the emission properties of the dust and the effective temperatures or bolometric magnitudes of stars in the H II regions, suggesting that the H II region evolutionary timescale is not on the order of the dust processing timescale. We find that the infrared emission of superbubbles and classical H II regions shows little differentiation between the two classes, despite the significant differences in age and morphology. We do detect a correlation of the 24 μm emission from hot dust with the ratio of 70–160 μm flux. This correlation can be modeled as a trend in the temperature of a minority hot dust component, while a majority of the dust remains significantly cooler.

Key words: dust, extinction – H II regions – ISM: bubbles

Online-only material: color figures

1. INTRODUCTION

The life cycle of interstellar dust remains a largely underconstrained process. Until recently, attempts to characterize the evolution of dust have been impeded by uncertainties regarding dust's composition, physical state, emission processes, and illuminating radiation field. All of these parameters must be known prior to drawing any observationally based conclusion on dust evolution, and before recent results from the *Spitzer Space Telescope* emerged, these parameters had been largely uncertain as well. A consensus is gradually forming around some of these properties, with the modeling of the "unidentified infrared bands" as vibrational emission from polycyclic aromatic hydrocarbons (PAHs; Leger & Puget 1984; Allamandola et al. 1985), and models of the size distribution and cross sections of the PAHs and small grains are now better defined (Li & Draine 2001).

Many *Spitzer* programs have taken advantage of these new dust models to provide insight on many different classes of objects. Previous works have characterized the dust content of entire galaxies (e.g., Dale et al. 2005; Draine et al. 2007) and individual star forming regions (e.g., Compiègne et al. 2008; Berné et al. 2007, among many others), but consistent analyses of larger samples of H II regions have been somewhat lacking. One exception is the work of Gordon et al. (2008), which used a sample of H II regions in M101 to probe metallicity-dependent dust processing. Their findings linked the ionization parameter of H II regions with a decrease in the PAH emission feature equivalent widths, which is evidence for the destruction of PAHs.

Our work seeks to relate the properties of the stars in H II regions to their dust content and emission. The radiation output from these massive, luminous stars dominates the heating of the dust, and the stellar SED and luminosity may affect the dust emission. Evolved massive stars are also thought to be an important source for dust production, and stellar wind shocks and supernovae (SNe) can also be important for processing dust. Our work leverages a previously compiled sample of H II regions with known spectral types for the ionizing stars. The sample includes regions with ages spanning from 1 to 5 Myr, including both classical H II regions and evolved, multi-SN superbubbles. This range of objects enables us to estimate the dust processing timescales. We seek to determine which of these varied parameters, if any, dominate the dust properties and emission. In Section 2, we describe the observations and data reduction; Section 3 contains our interpretation and modeling of the observed infrared ratios; Section 4 discusses the relation between stellar properties and infrared emission; and we explain the applicability of our work to other observations in Section 5.

2. SAGE OBSERVATIONS

Our sample of H II regions was drawn from the objects in Oey & Kennicutt (1997). The sample is listed in Table 1, with identifiers from Davies et al. (1976, hereafter DEM). The sample contains eight superbubbles and four classical H II regions, and all of the objects in this sample have spectroscopically determined spectral types for their ionizing stars. In Table 1, we have listed the spectral type of the hottest star in the association, which dominates the stellar luminosity and spectral energy

Table 1
Stellar Parameters for Target Objects

Name	Superbubble or Classical	Hottest Ionizing Star	Total Bolometric Magnitude	$n_\star^a$	L_{IR}/L_{bol}	Reference
DEM 25	S	O9 V	−8.88	10	0.058	Oey (1996)
DEM 31	S	WN6	−11.6	24	0.011	Oey (1996)
DEM 34	C	O3 III	−13.1	49	0.029	Parker et al. (1992)
DEM 50	S	O6.5 V	−10.7	12	0.073	Oey (1996)
DEM 106	S	O6.5 V	−11.4	16	0.055	Oey (1996)
DEM 152	S	O5 III	−12.4	64	0.087	Oey & Massey (1995)
DEM 192	S	WC5	−12.3	53	0.0071	Oey & Smedley (1998)
DEM 199	C	WR	−11.8	35	0.15	Garmany et al. (1994)
DEM 226	S	O6.5 V	−10.5	10	0.091	Oey (1996)
DEM 243	C	O9 V	−11.0	17	0.091	Oey (1996)
DEM 301	S	O3 I	−10.8	24	0.055	Oey (1996)
DEM 323	C	O3 III	−12.2	27	0.13	Massey et al. (1989)

Note.[a] The number of stars whose luminosities are summed to compute the total bolometric magnitude.

distribution in the region. We have also included the total stellar bolometric magnitude for the ionizing stars, determined by summing the luminosities of all stars spectroscopically observed by the work referenced in the last column. The bolometric corrections had been applied by the authors of each cited work except for DEM 199, for which we used the bolometric corrections of Martins et al. (2005) for O and B stars and Crowther (2007) for Wolf–Rayet stars. With the inclusion of superbubbles, our sample spans a wider range of object ages, which could potentially demonstrate dust evolution. Many of the superbubbles also have SNe and shocks which could drive dust processing.

The infrared data were obtained from the *Spitzer* Legacy program, Surveying the Agents of a Galaxy's Evolution (SAGE; Meixner et al. 2006). The program observed an area of $\sim 7^\circ \times 7^\circ$, covering the Large Magellanic Cloud (LMC) in all IRAC (3.6, 4.5, 5.8, and 8 μm) and MIPS (24, 70, and 160 μm) bandpasses. The individual observations were calibrated, combined, and mosaicked by the SAGE team, with a pipeline similar to that of the GLIMPSE survey (see Meixner et al. 2006; Benjamin et al. 2003, for further details).

2.1. Photometry

In order to compare surface brightnesses of the target objects at different wavelengths, it is necessary to convolve the images to the lowest resolution of the observations, which in our case is the 160 μm band (full width at half-maximum of 40″). Due to diffractive features in the instrument's point-spread function (PSF), such as Airy rings and spikes, a convolution with a Gaussian kernel would not produce sufficiently accurate results. Instead, we used the convolution kernels described in Gordon et al. (2008), which are calculated from model PSFs. This convolution also alleviates the need for aperture corrections when computing band ratios, since the aperture correction will be a constant factor for all bands.

We followed the prescription of Helou et al. (2004) for using the 3.6 μm images to remove the stellar flux from the 8 and 24 μm images. We computed the non-stellar flux (F_ν^{ns}) from the observed flux (F_ν) in each band using

$$F_\nu^{ns}(7.9\,\mu\mathrm{m}) = F_\nu(7.9\,\mu\mathrm{m}) - 0.232 F_\nu(3.6\,\mu\mathrm{m}) \quad (1)$$

and

$$F_\nu^{ns}(24\,\mu\mathrm{m}) = F_\nu(24\,\mu\mathrm{m}) - 0.032 F_\nu(3.6\,\mu\mathrm{m}), \quad (2)$$

where the coefficients are from Helou et al. (2004). These constants were determined by comparing the mid-infrared emission of stellar population synthesis models to their 3.6 μm emission. The infrared emission of these models is not strongly sensitive to star formation history or metallicity and should be generally applicable, but they are still approximate. Using the 3.6 μm images for this subtraction also assumes that the 3.6 μm band includes no dust emission, even though a small amount of dust emission is often present in this band. A visual check of the subtraction confirmed the efficacy of the subtraction at removing numerous faint point sources from the images. Since the contribution from stellar sources at 71 and 160 μm is negligible, we performed no correction on those bands. When discussing the 8 μm and 24 μm photometry in what follows, we will be referring to these corrected non-stellar fluxes.

We performed aperture photometry on the objects, with apertures defined by hand. In all cases, we set the apertures such that they included all of the Hα flux that could reasonably be associated with the target object. The Magellanic Cloud Emission-line Survey (MCELS; Smith & MCELS Team 1998) Hα imaging of the LMC was used for this comparison. Figure 1 shows infrared and Hα images of all of the superbubbles in our sample, and Figure 2 shows the classical H II regions. In both figures, the photometric apertures are outlined in white.

2.2. Background and Error Estimation

Our photometry is potentially contaminated by both diffuse emission from the Milky Way and by emission from unrelated dust in the LMC in the foreground or background of our objects (hereafter collectively referred to as "background" emission). We subtracted this background emission from our objects, measuring the background level with an annulus spanning 14–17 arcmin from the center of each region. We used the mode (the most commonly occurring value after binning the values into 0.01 MJy sr^{-1} bins) of the pixels in this annulus as the background level. The mode was chosen rather than the mean in order to reduce the sensitivity of the background estimation to bright structures from neighboring clouds. We note that it is impossible to completely account for emission unrelated to our objects that may appear within our target apertures, since much of the dust emission varies on size scales smaller than our apertures. Though this should not cause a systematic error in our photometry, it will still necessitate a level of caution in interpreting values for specific target objects.

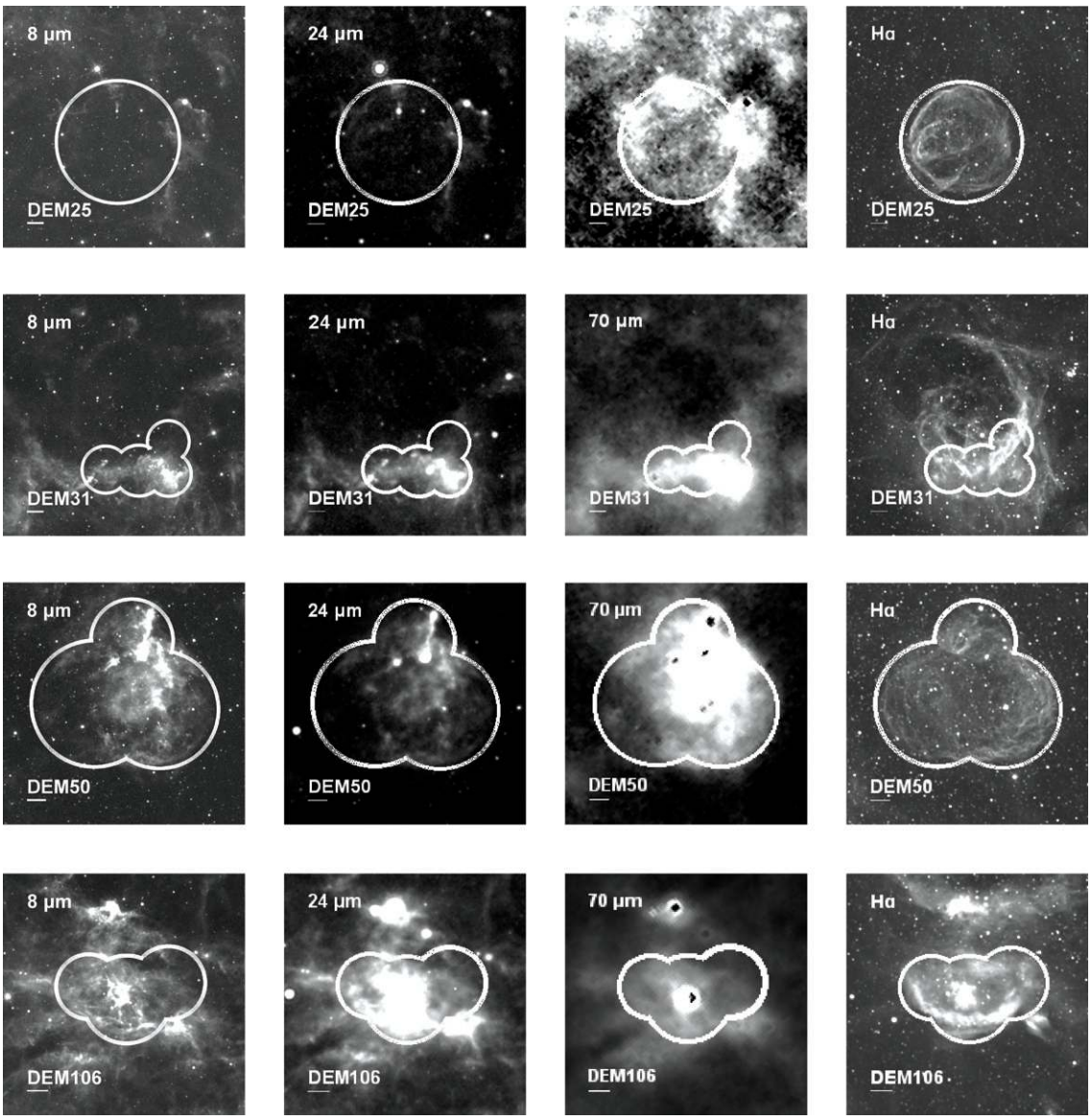

Figure 1. Images of the superbubbles in our sample in 8 μm, 24 μm, 70 μm and Hα, with our object apertures overlaid. The scale bar in the lower left of each image is 1 arcmin, corresponding to 15 pc at the distance of the LMC (52 kpc; Szewczyk et al. 2008).

Given that it is possible for this background contamination to exist despite our efforts to remove it, we would like to know the extent to which it may compromise our measurements. We therefore need to know the variance we would measure with our apertures if they were placed randomly and not on our target objects. By placing a number of "error estimation" apertures of the same size as our object apertures and measuring the variance in integrated light amongst them, we can thus obtain some estimate of the uncertainty in our photometry. This still does not allow us to measure the background's contribution to any single object's photometric measurement any better than we did with the background annulus, but it does inform us of the uncertainty in that measurement. The flux densities for all of our objects, corrected for stellar and background emission, are listed in Table 2. These flux densities have not had an aperture correction applied, so they are likely to be systematically low. This does not affect the band ratios used in this work though, since the necessary correction factors are identical for all bands as a result of convolving each image to a common PSF. Contamination by unremoved background is the dominant source of uncertainty in our photometry and the error bars on the figures and in Table 2 reflect that.

Table 2
Measured Infrared Fluxes for Target Objects

Name	IRAC4 8.0 μm (Jy)	MIPS24 24 μm (Jy)	MIPS70 70 μm (Jy)	MIPS160 160 μm (Jy)
DEM 25	2.2 ± 4.5	4.3 ± 2.5	87 ± 69	220 ± 200
DEM 31	2.9 ± 1.9	3.4 ± 1.4	230 ± 39	520 ± 89
DEM 34	1.4 ± 16	1.6 ± 13	35 ± 360	90 ± 1000
DEM 50	28 ± 4.8	28 ± 2.3	690 ± 48	1300 ± 130
DEM 106	45 ± 2.3	110 ± 2.0	870 ± 42	1600 ± 100
DEM 152	150 ± 8.6	530 ± 9.9	3900 ± 160	4300 ± 350
DEM 192	6.0 ± 1.4	23 ± 1.2	320 ± 25	390 ± 63
DEM 199	130 ± 24	440 ± 52	3800 ± 660	5300 ± 1100
DEM 226	24 ± 15	37 ± 18	760 ± 300	1200 ± 600
DEM 243	37 ± 6.8	84 ± 3.6	1100 ± 79	1900 ± 230
DEM 301	20 ± 3.3	30 ± 1.8	480 ± 57	1100 ± 140
DEM 323	120 ± 100	230 ± 100	3800 ± 1600	9700 ± 4300

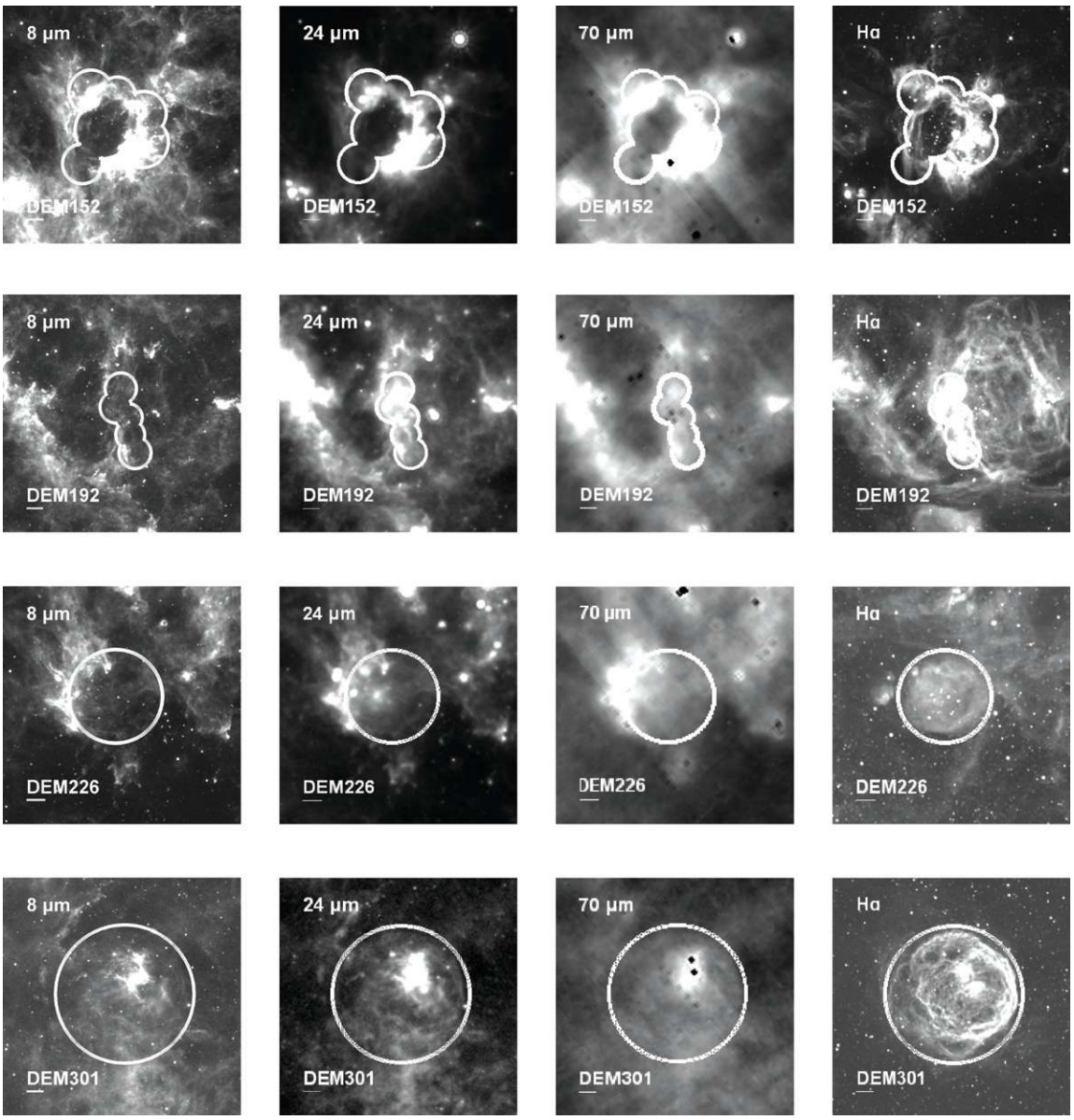

Figure 1. (Continued)

3. DUST EMISSION AND MODELING

To allow for comparisons between objects with different luminosities, we constructed three different flux ratios from the data, following the methods of Draine & Li (2007). These are

$$P_{7.9} = \frac{\nu F_\nu^{\rm ns}(7.9\,\mu{\rm m})}{\nu F_\nu(71\,\mu{\rm m}) + \nu F_\nu(160\,\mu{\rm m})}, \quad (3)$$

$$P_{24} = \frac{\nu F_\nu^{\rm ns}(24\,\mu{\rm m})}{\nu F_\nu(71\,\mu{\rm m}) + \nu F_\nu(160\,\mu{\rm m})}, \quad (4)$$

and

$$R_{71} = \frac{\nu F_\nu(71\,\mu{\rm m})}{\nu F_\nu(160\,\mu{\rm m})}. \quad (5)$$

$P_{7.9}$ is primarily a tracer of the aromatic emission commonly associated with PAHs, while P_{24} tends to trace hot, thermalized dust. Both of these are normalized by the total thermal dust emission, traced by the quantity $\nu F_\nu(71\,\mu{\rm m}) + \nu F_\nu(160\,\mu{\rm m})$. The ratio R_{71} measures the temperature of the dust that has reached thermal equilibrium, which is generally comprised of larger grains with radii greater than 100 Å. Since the temperature at which these grains equilibrate is determined solely by the amount of radiation they receive, the $70/160\,\mu$m ratio is also useful as a tracer of the total radiation content of the region.

Figure 3 shows the effect of radiation intensity on both the PAH and very small grain populations. The top panel shows that $P_{7.9}$ is largely uncorrelated with the total radiation content of the region. This is expected as the PAH emission is the result of stochastic heating of grains: the level of the PAH emission is directly proportional to the radiation intensity, but the overall PAH emission spectral shape does not vary with the radiation intensity (Draine & Li 2001). Since the ratio $P_{7.9}$ is normalized by the far-infrared emission ($\nu F_\nu(71\,\mu{\rm m})+\nu F_\nu(160\,\mu{\rm m})$) which is also proportional to the radiation content of the region, the ratio is therefore largely independent of the intensity of the radiation.

The lower panel in Figure 3 indicates that P_{24} ratio increases with radiation intensity. Since the $8\,\mu$m data show that PAH

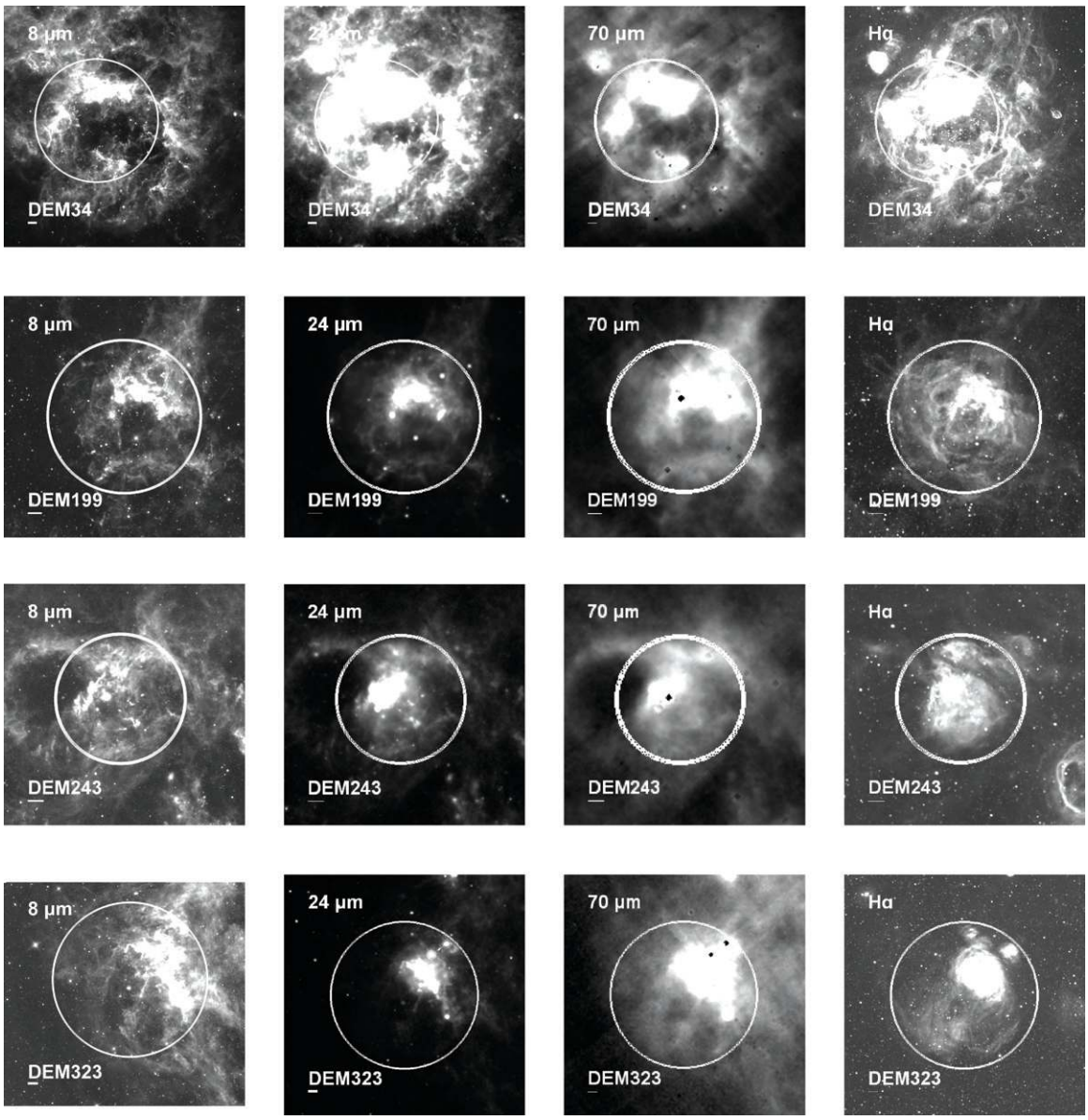

Figure 2. Same as Figure 1, but showing the classical H II regions in the sample.

emission is largely uncorrelated with the 70/160 μm ratio, it is clear that the trend in 24 μm must be the result of thermalized dust, rather than the PAH emission within the 24 μm bandpass. At low temperatures, the thermal dust emission is detected only in the 70 and 160 μm bands, but for dust exposed to high radiation intensities, the thermal peak can reach into the 24 μm band. We therefore hypothesize that as the overall luminosity of the region increases, the peak radiation intensity seen by the dust and consequently the temperature of the dust also increase in a correlated way.

Which parameter determines the position of an H II region along this 24 μm sequence, and which parameters determine the locus of the sequence itself? Since we hypothesize that this trend is driven by the effects of the illuminating radiation field, and not a change in dust composition, we examine parameterizations of the radiation that can best reproduce this correlation.

Our simple models of the sequence in 24 μm emission are shown in Figure 4. In this figure, we have plotted P_{24}–$0.14P_{7.9}$, which was suggested by Draine et al. (2007) as a way to remove the contribution of PAHs to the 24 μm band, and leave only the flux from thermalized grains. This minimizes any effects caused by variations in PAH abundances. Figure 4 shows the same tight correlation in this measure of the dust emission as that for P_{24} alone, uncorrected for PAH emission.

Using absorption cross sections and grain size distributions from Draine & Li (2007), we constructed a variety of models to compare to our observed sequence. Our models compute only the emission from the thermalized dust. In thermal equilibrium, the dust grain emission must equal absorption, hence

$$\int_0^\infty C_{\rm abs}(a,\lambda)u_\lambda\, d\lambda = \frac{4\pi}{c}\int_0^\infty C_{\rm abs}(a,\lambda)B_\lambda(T)\, d\lambda, \quad (6)$$

where $C_{\rm abs}(a,\lambda)$ is the absorption cross section as a function of grain radius a and wavelength λ, u_λ is the radiation energy density, and $B_\lambda(T)$ is the Planck function (Li & Draine 2001). We follow Draine & Li (2007) in parameterizing the radiation field as $u_\lambda = U u_\lambda^{\rm MMP83}$, where we use U as a scaling coefficient on the mean interstellar radiation field $u_\lambda^{\rm MMP83}$ from Mathis et al. (1983). This parameterization was chosen primarily to

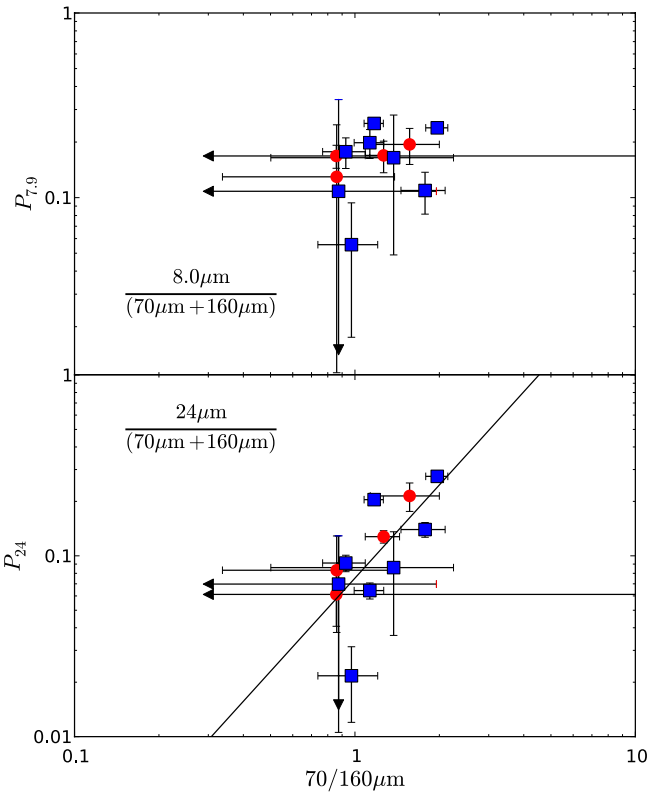

Figure 3. Top: PAH emission as a function of radiation intensity of the region, showing little correlation. Blue squares are superbubbles, while red circles are classical H II regions. Bottom: 24 μm emission shows a clear increase as the radiation content of the region increases. Symbols are as above, and the solid line is a fit to all points.

(A color version of this figure is available in the online journal.)

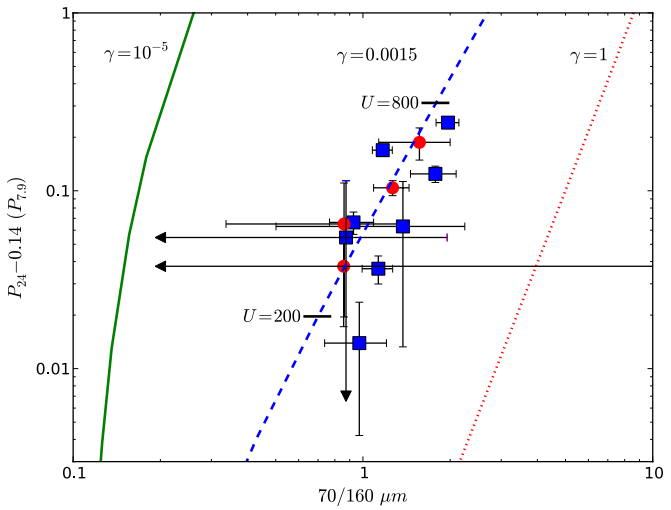

Figure 4. 24 μm thermal emission component shown against the 70/160 μm ratio. Superbubbles are blue squares, and classical H II regions are red circles. The best-fit dust model is shown by the blue dashed line, which contains a small fraction of hot dust determined by γ. The red dotted line shows a model where all of the dust is hot $\gamma = 1$, and the green solid line shows a model with only a miniscule fraction of hot dust ($\gamma = 10^{-5}$). Tick marks are shown on the best-fit model at $U = 200$ and $U = 800$ to give an idea of the range of radiation intensities (U) needed to span the observations.

(A color version of this figure is available in the online journal.)

aid comparison to other works; since the grain is assumed to reach an equilibrium temperature, only the energy content of the radiation field affects the dust emission and not the spectral energy distribution. For a given radiation field, we compute the temperature T for each grain size such that the equation of equilibrium (Equation (6)) is satisfied, then use that temperature to compute the infrared emission of the dust grain. We then sum this emission with the emission from grains of other sizes, using the size distribution from Li & Draine (2001).

In the simplest model, all of the dust in the H II region is heated by a single radiation intensity. We then computed a set of models spanning a range of radiation intensities (U), shown by the red, dotted line in Figure 4. This simple model shows that as the parameter U increases, the model's position in the R_{71}–P_{24} plot moves toward the upper right. This trend follows a similar slope to that of our observed set of H II regions, but the models exhibit a 70/160 μm ratio that is much higher than those of the observed regions. This suggests that though some dust must be exposed to high radiation intensities to reproduce the 24 μm emission, cold dust is also needed to reproduce the observed low 70/160 μm ratios. These dust components could be physically separate and have distinct temperatures, or they could form a continuum spanning a range of temperatures, but dust must be present at both high and low temperatures.

We therefore extend our models to include a mass fraction γ of dust exposed to high radiation intensities, and a mass fraction $(1-\gamma)$ that is exposed to a fixed low radiation intensity $U_{\rm min}$. We have adopted this parameterization from Draine & Li (2007), but note that we do not include the power-law distribution of radiation intensities that was used in their work; each of the dust components sees only a single radiation intensity. Namely, the dust is heated by two radiation intensities, with $(1-\gamma)\,U_{\rm min}$ of the total emission arising from the cold dust (heated by $U_{\rm min}$) and γU of the total emission arising from the hot dust (heated by U). We ran a grid of models over this parameter space (γ, $U_{\rm min}$) for a range of U and sought to minimize the chi-square between the models and the observations. The best-fitting model had the parameters $\gamma = 0.0015$ and $U_{\rm min} = 0.4$, shown by the blue, dashed line in Figure 4 and with tick marks indicating the position of $U = 200$ and $U = 800$ along the sequence. The small value of γ required to fit the observations suggests that the bulk of the dust inside our apertures is relatively cold, potentially originating from the photodissociation region (PDR) surrounding the ionized gas. This cold dust is at temperatures of roughly 15 K, but grains of different sizes equilibrate at different temperatures and thus there will be a range of dust temperatures. For comparison, grains exposed to $U = 600$ equilibrate between roughly 40 and 55 K.

It is important to remember that these models are merely suggestive, and cannot be considered a definitive explanation of the observed trend in P_{24}. We have here sought to explain the observations in terms of a single parameter model, where the only difference between objects is the maximum radiation intensity seen by a small fraction of the dust. It is worth noting that although we do not consider the derived parameters (γ, $U_{\rm min}$, U) to precisely represent the actual radiation intensities, the U values inferred from this simple model (i.e., $U > 100$) are indeed consistent with the premise that the 24 μm emission is mainly from dust attaining equilibrium temperatures. As shown in Figures 13 and 15 of Draine & Li (2007), at $U > 100$ the 24 μm emission is dominated by dust with equilibrium temperatures. The fact that such a simple model is able to reproduce the observed trend is certainly interesting, but should not be taken as a conclusive determination of the radiation field illuminating these objects. Our model is merely useful for illustrating that the

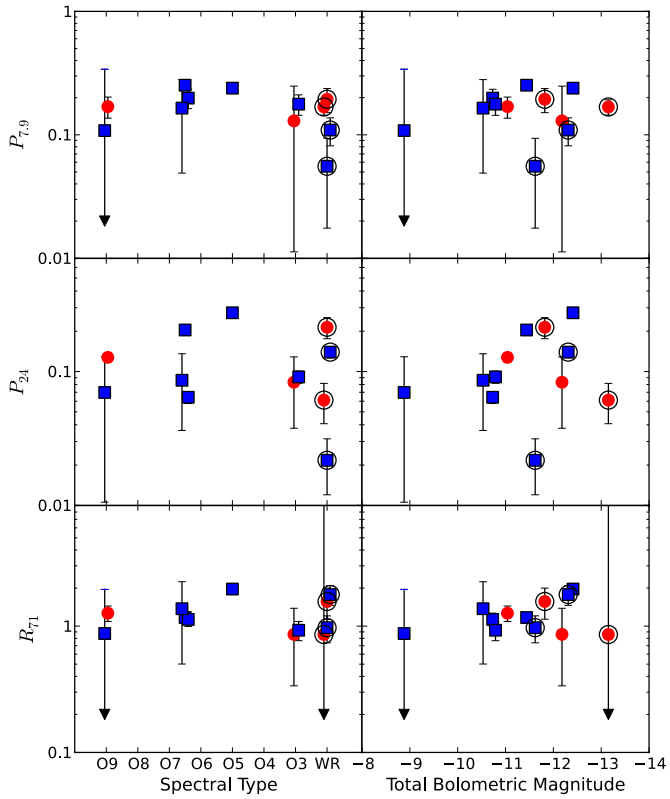

Figure 5. Infrared emission ratios are plotted against spectral type of the hottest ionizing star in each region (left), and against the total bolometric magnitude of massive stars in the region (right). Superbubbles are marked with blue squares, while non-superbubbles are marked with red circles. Objects that contain Wolf–Rayet stars are circled. Slight horizontal offsets have been added to points in the left panels for clarity.

(A color version of this figure is available in the online journal.)

observed sequence is set by the hottest dust component, and the temperature that this dust reaches determines the H II region's position along the sequence. Similarly, it is beyond the power of our data to suggest exactly what amount of dust is in the hot or cold components of the H II region itself since we could not definitively remove unrelated background or foreground emission from our measurements.

4. EFFECTS OF STELLAR PROPERTIES

Figure 5 shows our three infrared ratios plotted against the spectral type of the hottest ionizing star and the total bolometric magnitude of all the stars in the region. The top two panels show again that there is little systematic change in the PAH emission between objects. The center and lower panels can be used to diagnose the dust heating. What the data show is that neither the peak temperature nor the average temperature of the dust changes significantly as a function of stellar spectral type or total region luminosity.

This is not to say that the total dust emission is completely unaffected by the stellar luminosity; since they are both ratios they do not probe the total dust luminosity. Instead, the 70/160 μm ratio tells us that in regions with higher stellar luminosities, the dust does not have systematically higher temperatures. Looking at the effect of the bolometric luminosity on the 24 μm emission in the middle panel of Figure 5, we see that the stellar luminosity also does not influence the peak temperature of the dust. In Table 1, we have computed $L_{\rm IR}/L_{\rm bol}$, which is the ratio of the measured infrared emission (assuming 24, 70, and 160 μm bandpasses, but without correcting for emission outside these bands) to the bolometric luminosity of the stars in the region. Most of the regions have values of $L_{\rm IR}/L_{\rm bol}$ between 5% and 15%, though this is a lower bound and integrating over the entire infrared spectrum will yield higher values. The fairly constant value supports our picture that the total infrared emission necessarily increases to accommodate increased stellar emission but, as shown above, the dust temperature does not appear to be strongly affected.

We can estimate the temperature difference that would be expected from the range of bolometric luminosities spanned by our objects, using basic radiative equilibrium (Equation (6)), which implies that the stellar luminosity and dust temperature are related as $L_\star \propto T_{\rm dust}^4$, if the dust is like a black body. But because the far-infrared dust absorption cross section is approximately $C_{\rm abs} \propto \lambda^{-2}$, the dust temperature is actually related to the stellar luminosity by $L_\star \propto T_{\rm dust}^6$. Our objects span roughly a factor of 100 in luminosity, which corresponds to a factor of two increase in dust temperature. We therefore would only expect a modest trend in 70/160 μm, which would be further obscured by the large intrinsic scatter between objects. Note that this calculation also assumes that the dust in all objects is located the same distance from the illuminating stars. If the dust in more luminous regions was systematically closer or further from the stars, then the relative dilution of the radiation field may also affect emission.

5. DISCUSSION

It is important to highlight the fact that the correlation between the 70/160 μm ratio and 24 μm emission we have observed exists despite the numerous parameters of the H II regions that could affect their dust content and emission. Objects in our sample cover a wide range of morphologies and illuminating stellar sources. This could generate variations in the dust temperature distribution and resulting infrared emission, but this is not observed. Instead, the objects sit on a well-defined sequence with only minimal modification by geometric effects.

By including in our sample both classical H II regions and more evolved superbubbles, our sample also spans a range of ages. The superbubbles are generally older H II regions that have had time to evacuate a shell of material, and it would be reasonable to expect the dust in these objects to have undergone more processing than their younger counterparts. Additionally, superbubbles are often old enough for SNe to have occurred within them, which could affect the dust content. We do not observe any evidence of such effects, though, since in both 8 μm and 24 μm the two classes of objects exhibit no clear differentiation from each other. This could be a consequence of our significant photometric uncertainties, but is compatible with grain processing being completed on timescales shorter than the typical age of our classical H II regions (1–2 Myr), or on timescales longer than the typical age of the superbubbles (4–5 Myr).

Our results can also explain observations of H II regions in other galaxies. Galaxies in the *Spitzer* Infrared Nearby Galaxies Survey (SINGS) have exhibited a decreased 8/24 μm ratio in clumps corresponding to large H II regions, while the 8/160 μm ratio remains fairly smooth (Bendo et al. 2008). The 8/24 μm ratio is roughly a factor of two less in the clumps than it is in the rest of the galaxy, a factor which can be easily accounted for by our 24 μm observations. Our models therefore imply that the observed clumping in 8/24 μm can be explained by higher dust temperatures in these regions, without having to invoke

variation in dust abundance. Another study of SINGS galaxies by Calzetti et al. (2007) found that in the integrated light of galaxies there is correlation between 24 μm and Paschen α emission, which suggests that the 24 μm emission is indeed related to star formation. Similarly, starburst galaxies also show enhanced 24 μm emission that is attributed to hotter dust (e.g., Hanish et al. 2010).

Since our work deals only with the integrated light from the target objects, we are not able to distinguish between emission from the ionized region and emission from the PDR. Emission from PAHs has typically been found within the PDR and not the ionized region (Kassis et al. 2006), and consequently the properties of the H II region and the PAH emission may not be closely linked. We are also unable to say if the cold dust emission we observed is from the ionized region or the PDR. With its reduced radiation intensity, the PDR would be the logical source for the cold dust emission, but emission from the ionized region could be present as well.

Gordon et al. (2008) find a decrease in the PAH equivalent widths for H II regions as a function of their "ionization index," which is dominated by the ratio of [Ne III]/[Ne II] emission lines. The ionization index is directly linked to the temperature of the ionized gas, which could be responsible for the dust processing. We should see a similar effect in comparing our superbubbles, which have low ionization parameters due to geometric dilution of the radiation field, with our classical H II regions. But as described above, we find no systematic differences in 8 μm emission between the two classes of objects. Our objects span a comparable range of ionization parameters to the Gordon et al. (2008) objects, and it is thus surprising that all of our objects exhibit so little variation in $P_{7.9}$.

6. CONCLUSIONS

We find that the correlation between the 70/160 μm ratio and 24 μm emission is seen in both H II regions and superbubbles. We have qualitatively reproduced this trend with a simplified dust model that interprets this effect purely as the result of variations in the dust temperature between objects. That is, increasing an object's dust temperature alters its position in the P_{24}–R_{71} diagram (Figure 4) along the trend we observe. We therefore cannot infer grain processing or variation in grain composition.

Additionally, we do not detect any correlation between the dust emission ratios and the spectral type of the ionizing stars in the regions or the total luminosity of all stars in the region. There is also no differentiation in infrared emission between classical and superbubble regions, despite the significant differences in age, morphology, and ionization. This suggests that we are not observing processing or composition differences on the evolutionary timescale for superbubbles.

This research is based on observations made with the *Spitzer Space Telescope*, which is operated by the Jet Propulsion Laboratory, California Institute of Technology under contract with NASA. Support for this work was provided by NASA through an award issued by JPL, and by NSF grant AST-0806476. We thank K. Sellgren and A. Witt for helpful discussions, along with the anonymous referee for their insightful comments.

REFERENCES

Allamandola, L. J., Tielens, A. G. G. M., & Barker, J. R. 1985, ApJ, 290, L25
Bendo, G. J., et al. 2008, MNRAS, 389, 629
Benjamin, R. A., et al. 2003, PASP, 115, 953
Berné, O., et al. 2007, A&A, 469, 575
Calzetti, D., et al. 2007, ApJ, 666, 870
Compiègne, M., Abergel, A., Verstraete, L., & Habart, E. 2008, A&A, 491, 797
Crowther, P. A. 2007, ARA&A, 45, 177
Dale, D. A., et al. 2005, ApJ, 633, 857
Davies, R. D., Elliott, K. H., & Meaburn, J. 1976, MmRAS, 81, 89
Draine, B. T., & Li, A. 2001, ApJ, 551, 807
Draine, B. T., & Li, A. 2007, ApJ, 657, 810
Draine, B. T., et al. 2007, ApJ, 663, 866
Garmany, C. D., Massey, P., & Parker, J. W. 1994, AJ, 108, 1256
Gordon, K. D., Engelbracht, C. W., Rieke, G. H., Misselt, K. A., Smith, J.-D. T., & Kennicutt, R. C., Jr. 2008, ApJ, 682, 336
Hanish, D. J., Oey, M. S., Rigby, J. R., de Mello, D. F., & Lee, J. C. 2010, ApJ, 725, 2029
Helou, G., et al. 2004, ApJS, 154, 253
Kassis, M., Adams, J. D., Campbell, M. F., Deutsch, L. K., Hora, J. L., Jackson, J. M., & Tollestrup, E. V. 2006, ApJ, 637, 823
Leger, A., & Puget, J. L. 1984, A&A, 137, L5
Li, A., & Draine, B. T. 2001, ApJ, 554, 778
Martins, F., Schaerer, D., & Hillier, D. J. 2005, A&A, 436, 1049
Massey, P., Silkey, M., Garmany, C. D., & Degioia-Eastwood, K. 1989, AJ, 97, 107
Mathis, J. S., Mezger, P. G., & Panagia, N. 1983, A&A, 128, 212
Meixner, M., et al. 2006, AJ, 132, 2268
Oey, M. S. 1996, ApJ, 465, 231
Oey, M. S., & Kennicutt, R. C., Jr. 1997, MNRAS, 291, 827
Oey, M. S., & Massey, P. 1995, ApJ, 452, 210
Oey, M. S., & Smedley, S. A. 1998, AJ, 116, 1263
Parker, J. W., Garmany, C. D., Massey, P., & Walborn, N. R. 1992, AJ, 103, 1205
Smith, R. C., & MCELS Team, 1998, PASA, 15, 163
Szewczyk, O., et al. 2008, AJ, 136, 272